Herbicide-Degrading α-Keto Acid-Dependent Enzyme TfdA: Metal Coordination Environment and Mechanistic Insights[†]

Eric L. Hegg,[‡,§] Adam K. Whiting,[‡] Ruth E. Saari,[||] John McCracken,[*,⊥] Robert P. Hausinger,[*,||] and Lawrence Que, Jr.[*,‡]

Department of Chemistry and Center for Metals in Biocatalysis, University of Minnesota, Minneapolis, Minnesota 55455, Departments of Microbiology and Biochemistry, Michigan State University, East Lansing, Michigan 48824, and Department of Chemistry, Michigan State University, East Lansing, Michigan 48824

Received August 3, 1999; Revised Manuscript Received October 12, 1999

ABSTRACT: TfdA is a non-heme iron enzyme which catalyzes the first step in the oxidative degradation of the widely used herbicide (2,4-dichlorophenoxy)acetate (2,4-D). Like other α-keto acid-dependent enzymes, TfdA utilizes a mononuclear Fe(II) center to activate O_2 and oxidize substrate concomitant with the oxidative decarboxylation of α-ketoglutarate (α-KG). Spectroscopic analyses of various Cu(II)-substituted and Fe(II)-reconstituted TfdA complexes via electron paramagnetic resonance (EPR), electron spin−echo envelope modulation (ESEEM), and UV−vis spectroscopies have greatly expanded our knowledge of the enzyme's active site. The metal center is coordinated to two histidine residues as indicated by the presence of a five-line pattern in the Cu(II) EPR signal, for which superhyperfine splitting is attributed to two equivalent nitrogen donor atoms from two imidazoles. Furthermore, a comparison of the ESEEM spectra obtained in H_2O and D_2O demonstrates that the metal maintains several solvent-accessible sites, a conclusion corroborated by the increase in multiplicity in the EPR superhyperfine splitting observed in the presence of imidazole. Addition of α-KG to the Cu-containing enzyme leads to displacement of an equatorial water on copper, as determined by ESEEM analysis. Subsequent addition of 2,4-D leads to the loss of a second water molecule, with retention of a third, axially bound water. In contrast to these results, in Fe(II)-reconstituted TfdA, the cosubstrate α-KG chelates to the metal via a C-1 carboxylate oxygen and the α-keto oxygen as revealed by characteristic absorption features in the optical spectrum of Fe−TfdA. This binding mode is maintained in the presence of substrate, although the addition of 2,4-D does alter the metal coordination environment, perhaps by creating an O_2-binding site via solvent displacement. Indeed, loss of solvent to generate an open binding site upon the addition of substrate has also been suggested for the α-keto acid-dependent enzyme clavaminate synthase 2 [Zhou et al. (1998) *J. Am. Chem. Soc. 120*, 13539−13540]. Nitrosyl adducts of various Fe−TfdA complexes have also been investigated by optical and EPR spectroscopy. Of special interest is the tightly bound NO complex of Fe−TfdA·(α-KG)·(2,4-D), which may represent an accurate model of the initial oxygen-bound species.

α-Keto acid-dependent enzymes are the largest class of mononuclear non-heme iron oxygen-activating enzymes, catalyzing the oxidation of aliphatic C−H bonds in reactions that are even more diverse and varied (*1−3*) than those performed by the cytochromes P-450 and methane monooxygenase. The array of reactions catalyzed includes the posttranslational hydroxylation of amino acid side chains during collagen biosynthesis, the conversion of thymine to 5-hydroxymethyluracil in pyrimidine catabolism, the oxidative cyclization of proclavaminate in the biosynthesis of a clinically important β-lactamase inhibitor, and the synthesis of carnitine, a substance critical for both fatty acid anabolism and catabolism (*1−3*). The general reaction catalyzed by α-keto acid-dependent enzymes (Scheme 1) involves the oxidative decarboxylation of an α-keto acid cosubstrate, typically α-ketoglutarate (α-KG),[1] concomitant with the oxidation of the primary substrate (*2*). Detailed kinetic data on a number of α-keto acid-dependent enzymes indicate that they utilize an ordered binding mechanism, whereby iron binds first, followed by α-KG, and then either substrate or O_2, the order of which is enzyme dependent (*4−7*). The exact

---

[†] Financial support was provided by NIH grants GM33162 (L. Q.) and GM54065 (J. M.), an NIH postdoctoral fellowship for E. L. H. (GM18639), NSF grant MCB 9603520 (R. P. H.), and the Michigan State University Agricultural Experiment Station (R. P. H.).

[*] To whom correspondence should be addressed.

[‡] University of Minnesota.

[§] Present address: Department of Chemistry, University of Utah, Salt Lake City, UT 84112.

[||] Departments of Microbiology and Biochemistry, Michigan State University.

[⊥] Department of Chemistry, Michigan State University.

[1] Abbreviations: CS2, clavaminate synthase 2; 2,4-D, (2,4-dichlorophenoxy)acetate; DAOCS, deacetoxycephalosporin C synthase; EDTA, ethylenediaminetetraacetic acid; EPR, electron paramagnetic resonance; ESEEM, electron spin−echo envelope modulation; EXAFS, extended X-ray absorption fine structure; fwhm, full width at half-maximum; HPPD, 4-hydroxyphenylpyruvate dioxygenase; IPNS, isopenicillin N synthase; α-KG, α-ketoglutarate; MLCT, metal-to-ligand charge transfer; Mops, 4-morpholinepropanesulfonic acid; TauD, taurine/α-KG dioxygenase; TfdA, (2,4-dichlorophenoxy)acetate/α-KG dioxygenase.

10.1021/bi991796l CCC: $18.00 © 1999 American Chemical Society
Published on Web 11/18/1999

Scheme 1: General Reaction Performed by α-Keto Acid-Dependent Enzymes

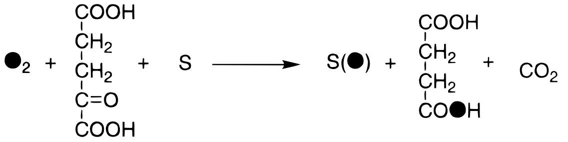

mechanism utilized by this class of enzymes, however, is currently unknown.

The crystal structures of two α-keto acid-dependent enzymes have recently been reported. Deacetoxycephalosporin C synthase (DAOCS), which catalyzes the transformation of penicillin N to deacetoxycephalosporin (*8*, *9*), contains a mononuclear iron center ligated to two histidines and an aspartate, while the structure of 4-hydroxyphenylpyruvate dioxygenase (HPPD), an enzyme involved in the catabolism of tyrosine, reveals a mononuclear iron coordinated to two histidines and a glutamate (*10*). These are the only endogenous ligands, which, in both cases, occupy a single face of the polyhedron. Interestingly, the active site of DAOCS and HPPD contain a number of structural features which are common to other crystallographically characterized mononuclear, non-heme iron enzymes including the extradiol ring-cleaving catechol dioxygenases 2,3-dihydroxybiphenyl 1,2-dioxygenase (*11*, *12*), catechol 2,3-dioxygenase (*13*), and protocatechuate 4,5-dioxygenase (*14*), the pterin-dependent tyrosine (*15*) and phenylalanine (*16*) hydroxylases, the Rieske-type naphthalene 1,2-dioxygenase (*17*), and isopenicillin N synthase (IPNS) (*18*). These common features include a "2-His−1-carboxylate facial triad" as the endogenous ligand set and the availability of three cis-oriented coordination sites for the binding of exogenous ligands (*19*) (Figure 1). An attractive hypothesis for the prevalence of this conserved structural motif in non-heme iron oxygen-activating enzymes is that the Fe(II) center has the flexibility to coordinate both substrate and O_2 (*19*). Furthermore, in contrast to heme enzymes, the cis-orientation of the available coordination sites on non-heme iron enzymes may allow intramolecular attack by the reactive oxygen species on the coordinated substrate (*19*).

The crystal structure of the DAOCS•(α-KG) complex has also been reported and reveals α-KG to be ligated to the iron center through a C-1 carboxylate oxygen and the α-keto oxygen (*9*). This binding motif, which was anticipated by biomimetic complexes (*20*−*22*) and has recently been proposed for α-KG binding to clavaminate synthase 2 (CS2) (*23*, *24*), maintains one available coordination site on the iron, presumably for coordinating O_2. Binding of O_2 to the Fe(II) center is proposed to generate a metal-coordinated superoxide which may then attack the α-carbon of α-KG to initiate oxidative decarboxylation and formation of a putative high valent iron−oxo species (*20*, *21*, *25*, *26*), the species postulated to be responsible for the subsequent oxidation reaction (Scheme 2).

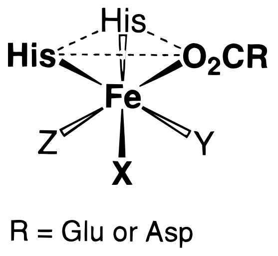

FIGURE 1: The 2-His-1-carboxylate facial triad utilized by many O_2-activating mononuclear non-heme iron enzymes.

Scheme 2: Proposed Reaction Mechanism for α-Keto Acid-dependent Enzymes

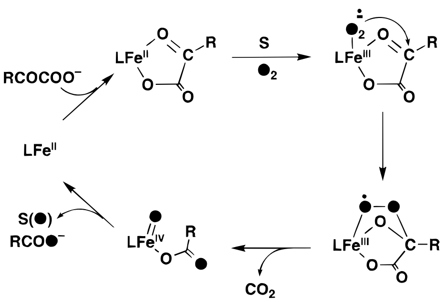

Scheme 3: Reaction Catalyzed by TfdA

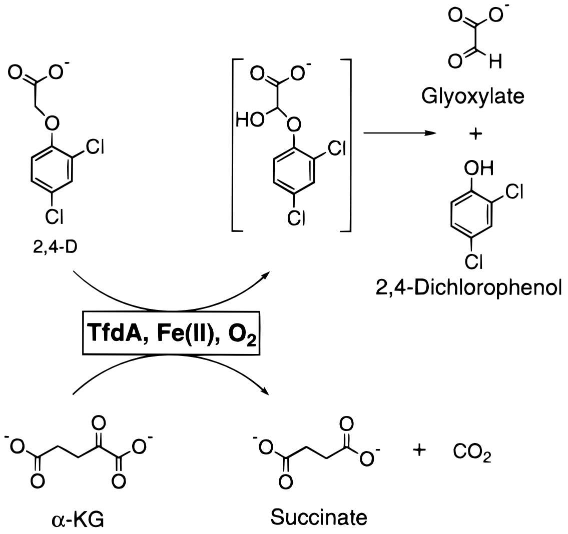

To gain further insight into the iron coordination environment and the mechanism of oxygen activation by α-keto acid-dependent enzymes, we have performed extensive spectroscopic studies on 2,4-dichlorophenoxyacetate/α-KG dioxygenase (TfdA). This enzyme catalyzes the first step in the biodegradation of the widely used herbicide 2,4-dichlorophenoxyacetate (2,4-D), as illustrated in Scheme 3 (*27*, *28*). TfdA possesses a His-X-Asp-$X_{(51)}$-His sequence motif (*29*), much like that found in IPNS and DAOCS; for the latter two enzymes these residues are known to function in metal ligation (*9*, *18*, *30*). While it is tempting to assume from the presence of this motif that TfdA also utilizes these same endogenous ligands, caution is warranted since TfdA displays very limited sequence homology to either of the other two enzymes. DAOCS, on the other hand, exhibits considerable sequence (20.6% identity and 32.2% similarity according to the comparison program GAP) and structural homology with IPNS (*9*). Therefore, understanding the iron coordination environment and mechanism of the herbicide-degrading TfdA has obvious importance not only in the area of bioremediation but also in the general understanding of how this varied and ubiquitous class of enzymes binds and activates dioxygen. We describe herein our spectroscopic studies on TfdA and place these results in perspective with other data recently obtained on this class of enzymes (*8*, *9*, *18*, *23*, *24*, *31*, *32*).

EXPERIMENTAL SECTION

Chemicals. Ferrous ammonium sulfate [$Fe(NH_4)_2(SO_4)_2$] and Mops were purchased from Sigma (St. Louis, MO), while 2,4-D, $CuCl_2 \cdot 2H_2O$ and the monosodium salt of α-KG were all obtained from Aldrich (Milwaukee, WI). Isotopically pure cupric oxide (^{63}CuO) was purchased from Cambridge Isotope Laboratories (Andover, MA). Argon and nitric oxide gas cylinders were obtained from Airgas, Inc. (Radnor, PA) and Matheson Gas Products, Inc. (Parsippany, NJ), respectively. All solutions were prepared with water, which was purified by passage through a Millipore (Bedford, MA) purification system.

Enzyme Isolation. The homodimeric 64 kDa enzyme TfdA was purified from *Escherichia coli* DH5α cells carrying the *Ralstonia eutropha* (formerly *Alcaligenes eutrophus*) JMP134 *tfdA* gene on a pUS311 plasmid as previously described (*27*). TfdA apoprotein was concentrated via centrifugation using Centricon-10 or Centricon-30 concentrators from Amicon. Buffer exchange was accomplished either via repeated concentration/dilution steps or using PD-10 desalting columns from Amersham Pharmacia Biotech (Wikströms, Sweden). Protein concentrations were ascertained using the Bio-Rad (Hercules, CA) assay utilizing bovine serum albumin as a standard. Alternatively, protein concentrations were assessed from the absorbance at 280 nm using a calculated (*33*) ϵ_{280} of 30 600 M^{-1} cm^{-1} per subunit (or 1.0 $AU_{280} \approx 0.96$ mg/mL) based on the amino acid sequence which contains 7 tyrosines, 4 tryptophans, and 13 phenylalanines (*29*).

Activity Assays. The specific activity of TfdA was assessed by reacting the product 2,4-dichlorophenol with 4-aminoantipyrine to give a colored product that was monitored spectrophotometrically (*27*). Alternatively, the activity was assayed by measuring O_2 uptake using a Gilson (Middleton, WI) model K-ICT C Oxygraph containing a 1.5 mL cell equipped with a YSI (Yellow Springs, OH) model 5331 Oxygen Probe, which reduces O_2 to water at the electrode surface; the oxygraph was calibrated by adding concentrated protocatechuate 3,4-dioxygenase to a known quantity of the substrate protocatechuate. Oxygen-uptake reactions were performed with an enzyme concentration of 1−10 μM subunit at 25 °C in 25 mM Mops buffer at pH 6.9. In a typical assay, anaerobic concentrated iron(II)-reconstituted TfdA was added to a stirring aerobic solution containing 66 μM α-KG, 0.33 mM 2,4-D, and 50 μM sodium ascorbate as a reductant.

Preparation of Cu−TfdA Samples. TfdA was reconstituted with copper by the slow addition of an aqueous $CuCl_2$ solution to TfdA apoprotein in 25 mM Mops buffer at pH 6.9 (rapid addition leads to some precipitation of protein). Substoichiometric amounts of copper (0.9 equiv/subunit) were added relative to the enzyme concentration, and electron paramagnetic resonance (EPR) spin quantitation indicated that all of the Cu^{2+} ions were bound to the enzyme. Samples containing α-KG and/or 2,4-D were prepared by the addition of 10 equiv of the appropriate substrate (in 25 mM Mops buffer at pH 6.9) to the Cu−TfdA solution. Typical sample concentrations were 500 μM TfdA subunit, 450 μM Cu^{2+}, 5.0 mM α-KG, and 5.0 mM 2,4-D. In cases where exogenous imidazole was added to the solution, the imidazole/copper ratio was maintained at 15. Isotopically pure [^{63}Cu]TfdA samples were prepared in an identical fashion except that $^{63}CuCl_2$ was prepared from ^{63}CuO by dissolving the cupric oxide in a minimal volume of concentrated HCl, then diluted with H_2O and adjusted to approximately pH 4 using NaOH(aq), yielding a final $^{63}CuCl_2$ stock concentration of 12 mM. Dual samples for electron spin−echo envelope modulation (ESEEM) spectroscopy were prepared in H_2O/D_2O at pH/pD 7.0 using $CuCl_2$ as described above except that the concentration of buffer was 50 mM and only 5 equiv of α-KG and 2,4-D were utilized.

Preparation of Fe−TfdA Samples. All samples were prepared anaerobically in an ice bath to prevent enzyme turnover, oxidative inactivation (*34*), and autoxidation of Fe^{2+}. TfdA solutions were made anaerobic by placing a small volume of concentrated TfdA (approximately 50−100 μL in 100 mM Mops buffer, pH 6.9 at 4 °C) in a heart-shaped Schlenk flask followed by two rapid vacuum/argon cycles. The enzyme was then allowed to equilibrate under Ar while stirring for approximately 15 min, followed by an additional 15 min of stirring under an Ar stream. All other solutions were prepared using standard Schlenk vacuum line techniques and contained 100 mM Mops buffer, pH 6.9, at 4 °C. TfdA apoprotein was reconstituted by the addition of a substoichiometric quantity of iron (0.8−0.9 equiv) from an ice-cold $Fe(NH_4)_2(SO_4)_2$ solution using gastight Hamilton syringes (Reno, NV). Samples containing α-KG and/or 2,4-D (5.0 equiv) were prepared by anaerobic addition of a concentrated buffered solution of the appropriate substrate to the Fe−TfdA solution. Typical TfdA concentrations ranged from 0.3 to 0.6 mM subunit for optical spectroscopy and 0.1 to 0.4 mM for EPR spectroscopy.

Preparation of NO Samples. Fe−TfdA solutions were briefly incubated with nitric oxide (NO) gas in either a Schlenk flask or Schlenk cuvette via headspace diffusion using standard Schlenk vacuum line techniques. The solutions were gently mixed until the samples exhibited the brillant yellow color characteristic of iron−nitrosyl complexes. Excess NO was removed by vacuum. To ensure that adventitous nitric acid was not introduced into the sample, the gas line was equipped with a column of NaOH pellets to "scrub" the NO and the line was purged with Ar for 30 min before using. ***Caution***: NO is a poisonous gas and should only be used with proper ventilation.

Electron Paramagnetic Resonance (EPR) Spectroscopy. X-band EPR spectra were recorded using either a Varian E−109 spectrometer or a Bruker E-500 spectrometer, both of which were equipped with an Oxford Instruments ESR-10 liquid helium cryostat. Samples were placed into 0.3 mm i.d. quartz tubes and frozen in liquid nitrogen. Cu−TfdA spectra were acquired at 20 K using a power of 0.20 mW. In general, the spectra were obtained as 4.0 min scans from 2200 to 2800 G using a time constant of 0.128 s, a modulation amplitude of 10 G, and a modulation frequency of 100 kHz. To obtain high-resolution spectra of the farthest downfield $\mathbf{g}_{\parallel}$ hyperfine line of Cu−TfdA, 4.0 min scans were obtained from 2560 to 2640 G using a time constant of 2.0 s, a modulation amplitude of 2.0 G, and a modulation frequency of 100 kHz. The high-resolution EPR spectra were fit using the program QPOWA (*35*). Nitrosyl Fe−TfdA spectra were collected as 168 s scans at 8.0 K from 0 G to 5000G at a power of 0.20 mW using a time constant of 0.164 s, a modulation amplitude of 10 G, and a modulation frequency of 100 kHz. Spin quantification of both Cu−TfdA and Fe−TfdA samples was performed by integrating the EPR absorption spectra and comparing the results with that of an aqueous CuEDTA solution of known concentration (*36*). In performing the spin quantifications, appropriate corrections were made for different EPR parameters between the standard and samples. In all cases, power saturation studies were performed to ensure that the signals were not saturated under the conditions utilized.

Electron Spin−Echo Envelope Modulation (ESEEM) Spectroscopy. Pulsed EPR data were collected on a home-built spectrometer as previously described (*37*). ESEEM data were collected in the usual point-by-point fashion using a Tektronix 620 B digital oscilloscope to perform signal averaging and numerical integration of the echo amplitudes. Data acquisition was controlled by a Power Computing model 200 computer, using software created with the LabView, version 5.0, programming package (National instruments). The microwave probe utilized a folded stripline resonant element (*38*) and a Gordon coupling scheme suitable for liquid helium immersion experiments (*39*). For two-pulse ESEEM experiments (90°−τ−180°), τ was varied from 150 ns to ~2.5 μs for each data set containing 512 points. Spectra were collected at 4.2 K using a microwave pulse power of 20 W, a pulse width of 20 ns (fwhm), and a repetition rate of 40 Hz. The magnetic field strength was set to 3050 G with a microwave frequency of approximately 8.8 GHz. Data analysis was performed using Matlab version 5.2 (Mathworks); dead time reconstruction (*40*) was used to process the data for the ESEEM envelopes prior to Fourier transformation. Computer simulations of deuterium ESEEM spectra were done using software based on the density matrix treatment of Mims (*41*).

Electronic Absorption Spectroscopy. Anaerobic Fe−TfdA samples were prepared as described above and placed in a 0.8 mL dual path length (2.0 mm × 1.0 cm) quartz cuvette (Wilmad Glass; Buena, NJ) which had been modified to contain a Schlenk-type fitting. Spectra were recorded on a scanning Beckman DU 640 spectrophotometer equipped with a refrigerated circulating bath. Typical enzyme concentrations (expressed as the number of active sites) were 0.3−0.6 mM. The reference sample contained only 100 mM Mops buffer. Spectra were obtained at 4 °C to stabilize the enzyme.

RESULTS

EPR Studies of Cu(II)-Substituted TfdA. To provide a means to probe the spectroscopically inaccessible Fe(II) active site and to circumvent the oxygen reactivity of Fe−TfdA, we replaced the native Fe(II) ion with Cu(II), an ion that possesses rich EPR properties and whose coordination chemistry is well characterized (*42*). Significantly, Cu(II) is a very strong competitive inhibitor of TfdA activity (K_i = 0.1−0.3 μM) with respect to Fe(II), suggesting that the Cu(II) ion replaces Fe(II) at the active site. In fact, the K_i of Cu(II) is significantly lower than the concentration of Fe(II) required for TfdA to achieve half-maximal activity (10−30 μM). Thus, while Cu(II) coordination is unlikely to exactly model that of Fe(II) due to the preference of Cu(II) for tetragonal geometries as opposed to the octahedral geometry common for Fe(II), analysis of the TfdA-bound copper environment is likely to reflect the important features of the native TfdA metallocenter.

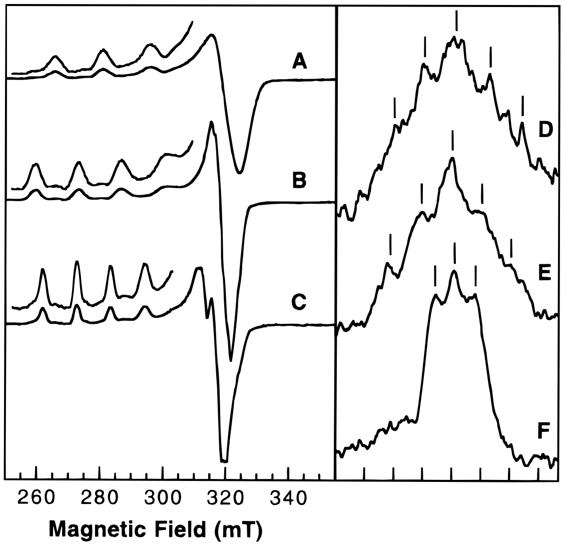

FIGURE 2: EPR spectra of Cu−TfdA complexes. (A) Cu−TfdA ($\mathbf{g}_\perp = 2.07$, $\mathbf{g}_\parallel = 2.29$, $A_\parallel = 16.1$ mK, 4.2 mT fwhm at 281 mT); (B) Cu−TfdA·(α-KG) ($\mathbf{g}_\perp = 2.07$, $\mathbf{g}_\parallel = 2.36$, $A_\parallel = 14.9$ mK, 4.2 mT fwhm at 273 mT); (C) Cu−TfdA·(α-KG)·(2,4-D) ($\mathbf{g}_x = 2.07$, $\mathbf{g}_y = 2.11$, $\mathbf{g}_z = 2.37$, $A_z = 12.0$ mK, 2.2 mT fwhm at 273 mT). Insets show $\mathbf{g}_\parallel$ with the intensity magnified 5 times. Spectra D−F display superhyperfine splitting of the $\mathbf{g}_\parallel$ region in [^{63}Cu]TfdA EPR spectra due to ^{14}N-containing (I = 1) ligands. While the spectra utilize different *x*-axes in order to align the peaks, each tick mark represents 1 mT for all three spectra. (D) [^{63}Cu]TfdA; (E) [^{63}Cu]-TfdA·(α-KG); (F) [^{63}Cu]TfdA·(α-KG)·(2,4-D). Spectra D−F were simulated with QPOWA (*33*) as described in the Experimental Section. Spectra D and E display 5-fold splitting (A = 1.0 mT) while spectrum F displays 3-fold splitting (A = 0.7 mT).

The EPR spectra of various copper-substituted TfdA complexes were obtained and have provided considerable insight into the nature of the endogenous ligands coordinated to the metal in the active site (*32*). In the absence of either the cosubstrate α-KG or the primary substrate 2,4-D (Figure 2A), Cu−TfdA exhibits an axial spectrum with **g**- and *A*-values ($\mathbf{g}_\perp = 2.07$; $\mathbf{g}_\parallel = 2.29$; $A_\parallel = 16.1$ mK)[2] consistent with the Cu(II) ion possessing tetragonal geometry (*43*) and a ligation environment containing a mixture of N and O donors (*44*). This EPR spectrum is perturbed by the addition of the cosubstrate α-KG (Figure 2B), with $\mathbf{g}_\perp = 2.07$, $\mathbf{g}_\parallel = 2.36$, and $A_\parallel = 14.9$ mK. While the addition of 2,4-D to Cu−TfdA has no effect on the EPR spectrum in the absence of α-KG, addition of 2,4-D to the binary Cu−TfdA·(α-KG) complex results in a more rhombic signal and a considerable sharpening of the spectrum from 4.2 mT (fwhm at 273 mT) to 2.2 mT (fwhm at 273 mT) with $\mathbf{g}_x = 2.07$, $\mathbf{g}_y = 2.11$, $\mathbf{g}_z = 2.37$, and $A_z = 12.0$ mK (Figure 2C). A comparison of the three spectra shows a progressive movement to lower field for $\mathbf{g}_\parallel$ and a decrease in the $A_\parallel$ values in the binary and ternary complexes. This is a significant trend since an

---

[2] A keiser (K) is equivalent in energy to a reciprocal centimeter (cm^{-1}). Therefore, using the units of K, $A_\parallel$ = (**g**-value) × (splitting in gauss) × (β_e).

increase in $\mathbf{g}_{\|}$ is usually indicative of a shift to a more oxyanion-rich environment (*44*), while small $A_{\|}$ values suggest a significant distortion from planarity (*45*, *46*). For example, the $\mathbf{g}_{\|}$ and $A_{\|}$ values of the ternary Cu−TfdA·(α-KG)·(2,4-D) complex are comparable to those of Cu-substituted ribulose-1,5-bisphosphate carboxylase/oxygense complexed to the transition-state analogue 2-carboxyarabinitol bisphosphate [$\mathbf{g}_{\|} = 2.41$, $A_{\|} = 11.59$ mK (*47*)] and Cu(II)-substituted enolase complexed to 2-phosphoglycerate [$\mathbf{g}_{\|} = 2.40$, $A_{\|} = 12.0$ mK (*48*)], both with crystallographically determined structures which reveal an oxyanion-rich environment at a distorted metal center (*49*, *50*).

In a previous communication (*32*), we incorrectly reported that the EPR spectra of Cu−TfdA·(pyruvate) complexes were identical to those with α-KG. This observation led to the erroneous conclusion that the C-5 carboxylate was not important in eliciting the characteristic spectrum of the Cu−TfdA·(α-KG) species. We have since discovered, however, that the pyruvate utilized in the experiments contained small quantities of a "pyruvate dimer" (2-hydroxy-2-methyl-4-oxoglutaric acid), which mimics α-KG in possessing the second carboxyl functional group. On the basis of its structural similarity to α-KG ($K_m = 3.2\ \mu$M), this "dimer" is presumed to have a much lower K_m than pyruvate ($K_m = 1.0$ mM). Experiments using authentic "pyruvate dimer" (synthesized by treating pyruvate with concentrated NaOH for at least 30 min) yielded the EPR spectrum characteristic of the α-KG-bound state, whereas those using ultrapure pyruvate failed to reproduce this spectroscopic feature. Thus, the C-5 carboxylate is, in fact, important in the binding of α-KG despite the fact that this carboxylate presumably does not coordinate to the metal center.

Further information about the coordination environment of the metal center was obtained from analysis of the superhyperfine splitting in the EPR spectra. This phenomenon arises from the interaction of the unpaired electron on the Cu(II) ion with the nuclear spin (I) of an atom directly bound to the metal and lying in the principal tetragonal plane (superhyperfine splitting is not observed for axial ligands). In an ideal situation, one can determine the number of nitrogen-containing ligands (while ^{16}O does not have a nuclear spin, ^{14}N has $I = 1$) since the number of superhyperfine lines is equal to $2nI + 1$, where n is the number of equivalent nuclei. An excellent example of such an analysis of superhyperfine splitting was recently reported by Ballou and co-workers in their study of Cu(II)-substituted phthalate dioxygenase (*51*).

Although not readily apparent from Figure 2, superhyperfine splitting is present in the $\mathbf{g}_{\perp}$ region of the Cu−TfdA EPR spectra, and this splitting can be discerned in the second derivative spectra. Figure 3A shows the EPR second derivative spectrum of Cu−TfdA in the $\mathbf{g}_{\perp}$ region. Unfortunately, the resolution of ligand superhyperfine features is poor, indicating that the structure about the metal center may be somewhat heterogeneous prior to substrate addition. When α-KG binds to the holoenzyme, however, the resolution of the superhyperfine features is greatly enhanced, and an apparent 1:2:3:2:1 quintet is observed (Figure 3C), consistent with two nitrogen-containing endogenous ligands. Enhanced resolution of the ligand superhyperfine features at $\mathbf{g}_{\perp}$ is also observed in the presence of a 15-fold excess of imidazole (Figure 3B). The appearance of at least nine features in this spectrum is commensurate with the addition of 1−2 exogenous imidazole ligands to the Cu(II) tetragonal plane, in addition to the two derived from the protein (*32*). These results suggest that TfdA maintains solvent-accessible sites on the metal ion which are presumably available for the binding of exogenous ligands.

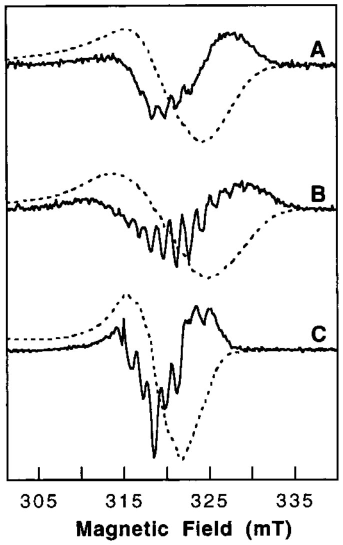

FIGURE 3: Superhyperfine splitting of the $\mathbf{g}_{\perp}$ region in Cu−TfdA EPR spectra due to ^{14}N-containing ($I = 1$) ligands. (A) Cu−TfdA; (B) Cu−TfdA in the presence of 15 equivalents of imidazole; (C) Cu−TfdA·(α-KG). The dashed lines are the expanded first derivative $\mathbf{g}_{\perp}$ signals, while the solid lines are the second derivative $\mathbf{g}_{\perp}$ signal in which the superhyperfine splitting is more easily observed.

The breadth of the $\mathbf{g}_{\perp}$ feature as shown in the second derivative spectra of Figure 3, however, indicates that $A_{\perp}^{\mathrm{Cu}}$ is similar in magnitude to the nitrogen superhyperfine splitting of the equatorially bound histidyl or imidazole ligands. This renders an analysis of the number of nitrogen-based ligands based on counting superhyperfine features at $\mathbf{g}_{\perp}$ tenuous and led us to a detailed examination of ligand superhyperfine structure in the $\mathbf{g}_{\|}$ region. Splitting in this region is often difficult to resolve because natural abundance copper contains a mixture of ^{63}Cu (69%) and ^{65}Cu (31%), both of which are $I = 3/2$ nuclei but give rise to slightly different $A_{\|}$ values. To increase the likelihood of observing the superhyperfine splitting, isotopically pure Cu(II) was utilized. The farthest downfield $\mathbf{g}_{\|}$ signal of samples prepared with [^{63}Cu]TfdA (Figure 2) exhibits improved resolution relative to that obtained using natural abundance copper and provides information complementary to that derived from the $\mathbf{g}_{\perp}$ region. For Cu−TfdA, a 1:2:3:2:1 pattern expected from two equivalent nitrogens may be discerned (Figure 2D). This five-line pattern is more clearly resolved in the Cu−TfdA·(α-KG) complex (Figure 2E), supporting the coordination of two nitrogen-containing ligands to the metal center. In the presence of both α-KG and 2,4-D (Figure 2F), however, the EPR spectrum displays only 3-fold splitting, indicating a loss of one of the nitrogen ligands from the tetragonal plane of Cu(II). These results suggest that 2,4-D binding either displaces one of the His ligands or causes a reorientation of the principal tetragonal plane of the Cu(II) ion such that one of the nitrogen ligands shifts to an axial position.

ESEEM Spectroscopy of Cu(II)-Substituted TfdA. To gain further information on the number and identity of the metallocenter ligands, Cu−TfdA samples were also studied by the ESEEM method of pulsed EPR spectroscopy. Previous ESEEM studies on this system provided evidence for the equatorial ligation of two His ligands for Cu−TfdA and the Cu−TfdA·(α-KG) adduct (*32*), in agreement with the results of continuous wave EPR experiments presented above. The ESEEM from one of these His ligands was lost upon the addition of 2,4-D to the Cu−TfdA·(α-KG) complex, consistent with the observed decrease in the multiplicity of the superhyperfine splitting in the ternary Cu−TfdA·(α-KG)·(2,4-D) complex. Because the model for Fe(II) coordination in this class of enzymes calls for the coordination of multiple water ligands that are displaced as the cosubstrates bind to the metal, ESEEM experiments were performed on samples exchanged against D_2O. The overall strategy for these measurements makes use of the product rule for ESEEM, which states that the modulation function for a discrete paramagnetic center consists of a product of a background decay function, governed by spin relaxation processes, with the individual modulation functions due to all of the coupled nuclei (*52*, *53*). If ESEEM data collected for samples exchanged against D_2O-based buffer are divided by ESEEM data collected under identical conditions for like samples in aqueous buffer, the resulting modulation function will contain only contributions arising from exchangeable deuterons that are magnetically coupled to the paramagnet (*54*). This technique thus provides a method to study coordinated water molecules in the presence of substantial ESEEM from the remote nitrogens of the coordinated histidyl ligands (*55*).

ESEEM ratios taken for Cu−TfdA, Cu−TfdA·(α-KG), and Cu−TfdA·(α-KG)·(2,4-D) are shown as solid lines in panels A−C of Figure 4, respectively. These data were collected using a two-pulse (90°−τ−180°−τ−echo) microwave excitation scheme because this method provides the most reliable measure of amplitudes for dividing data sets (*54*). Also, the two-pulse data feature a sum combination frequency component that provides an "internal" line width, or damping standard for distinguishing bound D_2O molecules from ambient waters (*55*). For all three enzyme samples, the data of Figure 4 show intense modulations that consist of major frequency components at 2.0 MHz (modulation period = 500 ns), the Larmor frequency of deuterium in a 0.305 T magnetic field, and a sum combination frequency centered at 4.1 MHz (modulation period ≈ 250 ns). In agreement with the proposal that the cosubstrates displace water ligands when they bind to Cu(II), the depth, or amplitude, of the modulations decreases as one goes from the Cu−TfdA data (Figure 4A) to the data for the Cu−TfdA·(α-KG)·(2,4-D) ternary complex (Figure 4C). Some caution needs to be taken when considering these results, however, since the ^{2}H-ESEEM shown in Figure 4 originates from D_2O molecules bound to the metal, ambient D_2O molecules close enough to the Cu(II) to magnetically couple to it, and deuterons that have exchanged with the exchangeable protons of TfdA near the metal site.

A useful means to differentiate the different populations of deuterons that contribute to the ESEEM is to make use of the relative amplitudes of the ^{2}H fundamental and sum combination frequency components. Figure 5 shows two-pulse ESEEM simulations for D_2O molecules bound to Cu(II) at an equatorial position (trace A) and an axial position (trace B). Figure 5C shows the predicted two pulse ESEEM for a D_2O molecule with both deuterons positioned 4 Å away from the Cu(II) and coupled by a dipolar, or through-space mechanism. The hyperfine splitting constants used for these simulations were taken from a single-crystal ENDOR study of $Cu(II)(H_2O)_6$ in Tutton salts and are given in the figure caption (*56*). Figure 5A shows a deuterium ESEEM pattern that features intense modulation at the deuterium Larmor frequency (2.0 MHz) which damps quickly and leaves only modulations at the sum combination frequency (4.1 MHz) at longer times. The axially bound D_2O (Figure 5B) shows deep modulations, but the fundamental frequency is less damped than it was for the equatorial case so that the second harmonic is less prominent at longer values of τ. The ambient water shows modulations that are a factor of 7−8 less intense than those of the bound waters with a substantially reduced contribution of the sum combination frequency (Figure 5C). These effects are conveniently viewed in the frequency domain as shown in Figure 6 where Fourier transforms of the simulations for equatorial (Figure 6A), axial (Figure 6B), and ambient (Figure 6C) D_2O molecules are provided. For equatorially bound D_2O, the anisotropic contribution to the hyperfine splitting is large (the effective dipole−dipole distance is about 2.4 Å), and that serves to broaden the width of the 2.0 MHz peak. Because the deuterium hyperfine splitting is of opposite sign in the two-electron spin manifolds

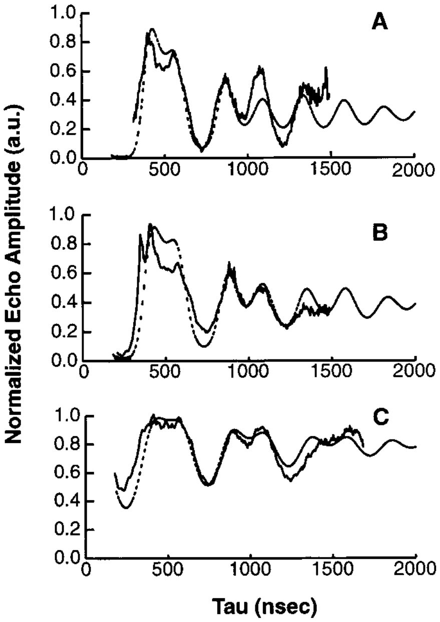

FIGURE 4: The solid lines are deuterium ESEEM data collected for (A) Cu−TfdA, (B) Cu−TfdA·(α-KG), and (C) Cu−TfdA·(α-KG)·(2,4-D). These data were obtained by dividing the two-pulse ESEEM data collected for each sample exchanged against D_2O-based buffer with the identical sample in H_2O-based buffer. Prior to division, each data set was normalized so that the ordinate ranged 0−1, where 0 amplitude was measured directly for each scan and 1 was assigned to the maximum amplitude found experimentally. Conditions common to these measurements were microwave frequency, 8.78 GHz; magnetic field strength, 0.305 T; microwave pulse power, 25 W; pulse width, 20 ns (fwhm); pulse sequence repetition rate, 40 Hz; 40 events were averaged at each time point and four complete scans were averaged to arrive at each ESEEM trace. The dashed lines are ESEEM simulations for (A) two equatorial and one axial bound D_2O molecules, (B) one equatorial and one axial bound D_2O, and (C) one axially bound D_2O. Simulations used the Hamiltonian parameters for equatorial and axial bound D_2O molecules given in the captions for Figure 5, respectively.

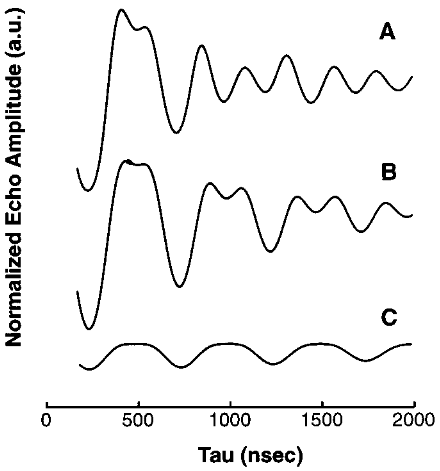

FIGURE 5: ^{2}H-ESEEM simulations for (A) a D_2O molecule bound equatorially to Cu(II), (B) an axially bound D_2O, and (C) a D_2O molecule coupled through space to Cu(II) so that the deuterium−copper distance was 4 Å. Hamiltonian parameters for the ESEEM simulations were for equatorially bound D_2O; $A_{xx} = -1.4$ MHz, $A_{yy} = -0.6$ MHz, $A_{zz} = 1.4$ MHz, nuclear **g**-value = 0.857 44, magnetic field = 0.305 T, starting $\tau = 180$ ns, $e^2qQ = 0.2$ MHz, nqi asymmetry parameter = 0.5 and the nqi and hyperfine tensors were taken as coaxial. Parameters were the same for the axially bound D_2O except for the hyperfine splitting, $A_{xx} = -0.5$ MHz, $A_{yy} = -0.5$ MHz, and $A_{zz} = 1.1$ MHz. For ambient D_2O (trace C), $A_{xx} = -0.2$ MHz, $A_{yy} = -0.2$ MHz, and $A_{zz} = 0.4$ MHz.

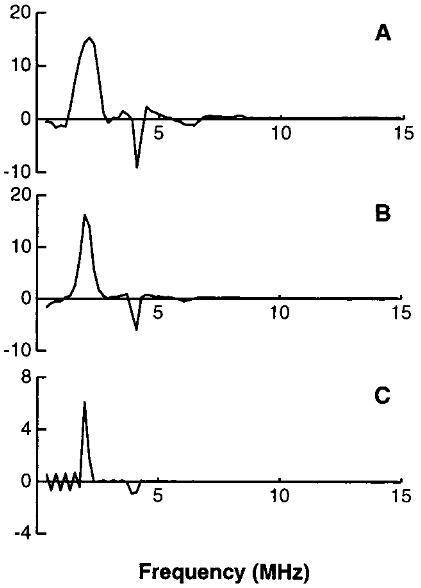

FIGURE 6: Fourier transforms of the ESEEM simulations shown in Figure 5. Trace A is for an equatorially bound D_2O, trace B an axially bound D_2O, and trace C ambient D_2O.

that combine to yield the sum combination peak, the width of the 4.1 MHz line remains narrow for all three of the splitting cases depicted in Figures 5 and 6. This feature is broadened only by the small nuclear quadrupole interaction that is intrinsic to the D_2O molecule.

The simulations of Figures 5 and 6 suggest that a simple method to gauge the relative contributions of equatorial and axial water coordination to Cu(II) ESEEM data is to determine the ratio of the amplitudes of first and second harmonics of the deuterium modulation frequencies as measured from the ESEEM spectra. For the simulation of equatorially bound D_2O (Figures 5A and 6A), this ratio is 1.5; for axially bound D_2O (Figures 5B and 6B), the 2/4 MHz intensity ratio climbs to 2.5; and for ambient water at 4 Å, a ratio of >5 is found. Table 1 shows the results of determining these ratios for simulations carried out for several cases of mixed equatorial/axial D_2O ligation. It is apparent that if both equatorial and axial D_2O ligands are present, the 2/4 MHz amplitude ratio is close to 2.0, a value that is intermediate to those representing pure axial or equatorial ligation. The chief source of errors in measuring peak amplitudes and computing these ratios comes from the reduced frequency resolution realized for 2-pulse ESEEM and difficulties in estimating the position of the baseline for each peak. The sum combination frequency can be measured more reliably because of its narrow line width and negative phase. In contrast, it is often difficult to estimate the baseline position for the low ^{2}H fundamental frequency because the baseline “roll”, which stems from shortcomings of the dead-time reconstruction procedure (*40*), is most severe near “0” MHz. The error for computing these peak ratios from the FT is probably ±0.1, for the simulations, and ± 0.2, for the experimental data of Figure 4.

Table 1: Ratios of ^{2}H-ESEEM Fundamental (2 MHz) and Sum-Combination (4 MHz) Frequencies for Various D_2O Coordination Schemes

(A) Computer Simulations

coordinated D_2O molecules	2/4 MHz ratio
2 equatorial, 0 axial	1.5 (±0.1)
1 equatorial, 0 axial	1.5
2 equatorial, 1 axial	1.7
1 equatorial, 1 axial	1.7
2 equatorial, 2 axial	2.0
1 equatorial, 2 axial	2.0
0 equatorial, 1 axial	2.5
0 equatorial, 2 axial	2.5

(B) TfdA Data

sample	2/4 MHz ratio
Cu-TfdA	1.7 (±0.2)
Cu-TfdA•(α-KG)	1.8
Cu-TfdA•(α-KG)•(2,4-D)	2.5

The 2/4 MHz amplitude ratios measured from Fourier analysis of the three TfdA ^{2}H-ESEEM traces of Figure 4 are also listed in Table 1. The ternary complex Cu−TfdA•(α-KG)•(2,4-D) gives a ratio of 2.5, indicating that it has at least one axially bound D_2O ligand and no equatorial waters. For the other two complexes, Cu−TfdA and Cu−TfdA•(α-KG), more ^{2}H second harmonic is observed with these 2/4 MHz peak ratios being 1.7 and 1.8, respectively. These results favor a model for Cu(II) water coordination that begins with two equatorial waters and one axial water for the protein in the absence of the cosubstrates (Cu−TfdA). The addition of α-KG displaces one of the equatorial water molecules to leave one equatorial and one axial water. Finally, formation of the ternary complex leads to the displacement of the remaining equatorial water to yield a Cu(II) site with a single, axially bound water molecule. To test this idea, ^{2}H-ESEEM calculations were carried out using the model simulations of Figure 5, curves A and B, together with the spherical model approximation to the ESEEM product rule (*57*) to produce simulations of the two-equatorial/one-axial, one-equatorial/one-axial, and one-axial cases. The results are superimposed on the data of panels A−C of Figure 4, respectively (dashed lines) and show that there is good agreement between the measured ^{2}H-ESEEM functions (solid lines) and the amplitudes predicted theoretically. No attempt was made to adjust the hyperfine parameters from the values determined in the single-crystal ENDOR studies of Cu(II)(H_2O)$_6$ in Tutton salts (*56*).

There are several features of the ^{2}H-ESEEM data shown in Figure 4 that need to be kept in mind when judging the quality of the simulations. These data were obtained by dividing two sets of 2-pulse ESEEM data that featured deep ^{14}N modulations from His coordination and background decay functions due to electron spin−spin relaxation that left only small amplitudes at longer τ. As a result, one is forced to take the ratios of small numbers adding considerable noise to the result that gets worse at longer times. The data shown in Figure 4 are truncated at 1500 ns because the noise in the ratio becomes too severe at higher τ values. The agreement between experiment and theory is worst for the Cu−TfdA sample (solid line of Figure 4A) because the deeper ^{2}H modulation that results from the additional bound water molecule leads to greater uncertainty in the ratio, and additional ambient water, that likely has access to the site when the cosubstrates are absent, is not being considered in the calculation. As a result of these problems, emphasis was placed on comparison between experiment and theory for the first 1 μs of the ^{2}H-ESEEM function of Figure 4A, providing strong evidence that there are two equatorial and one axial D_2O molecules bound to the Cu(II) of TfdA in the absence of the cosubstrates.

In principle, further verification of our ^{2}H-ESEEM modeling of water coordination to Cu−TfdA could be obtained by taking another set of ESEEM ratios. By dividing the ratio of Figure 4A with that of Figure 4B, it should be possible to obtain the ^{2}H-ESEEM pattern of the water displaced by α-KG binding. In a similar fashion, division of Figure 4B by Figure 4C should reveal the ^{2}H-ESEEM function of the D_2O molecule displaced by 2,4-D addition to the protein. Unfortunately, this procedure is only accurate when the continuous wave EPR spectrum remains unchanged as a result of substrate addition. Because there are large changes that occur when adding α-KG to Cu−TfdA, particularly with respect to narrowing the distribution of coordination environments that likely exists for the holo-enzyme, the ratio of trace B in Figure 4 with trace A gave a deep ^{2}H-ESEEM pattern with a 2/4 MHz ratio of 1.1 and an appearance that was much different from the model calculations of Figure 5, traces A and B (data not shown). However, the changes in the EPR spectrum that occur when 2,4-D is added to the Cu−TfdA·(α-KG) complex are more subtle, and a good ratio was obtained by dividing the ^{2}H-ESEEM data of Figure 4, trace B, with that of trace C. The result provides the ^{2}H-ESEEM spectrum of the D_2O displaced by 2,4-D addition and is shown in Figure 7 (solid line). The dashed line superimposed on these data is from the model calculation of the ^{2}H-ESEEM for a D_2O molecule bound equatorially to Cu(II).

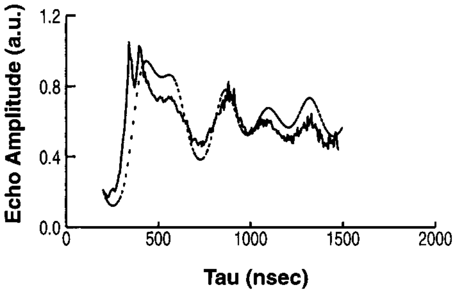

FIGURE 7: The solid line is a ^{2}H-ESEEM trace obtained by dividing the experimental ratios for Figure 4B by that of Figure 4C. The dashed curve is a simulation for a single D_2O molecule bound equatorially to Cu(II) and was obtained by truncating the trace of Figure 5A at 1.5 μs.

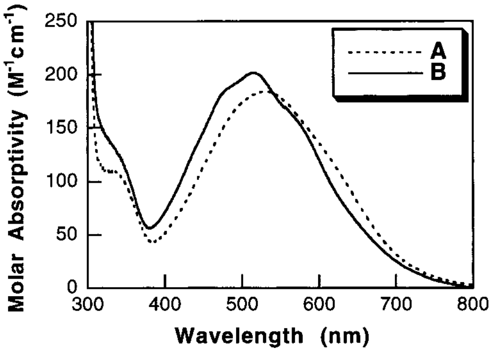

FIGURE 8: Optical absorption spectra of (A) Fe−TfdA·(α-KG) (λ_{max} = 530 nm) and (B) Fe−TfdA·(α-KG)·(2,4-D) (λ_{max} = 515 nm with shoulders at approximately 475 and 560 nm). The spectrum of the Fe−TfdA sample has been subtracted to minimize protein scattering effects.

Binding of α-KG and 2,4-D to Fe(II)-Reconstituted TfdA. Binding of α-KG to the metal center was assessed directly via optical spectroscopy. In the absence of α-KG, the optical spectrum of Fe−TfdA does not exhibit any absorption features in the visible region, while the UV region is dominated by protein $\pi-\pi^*$ transitions. Lack of a visible chromophore is typical of high-spin Fe(II) species. Upon the anaerobic addition of α-KG, however, the enzyme solution becomes pinkish and a broad absorption is observed in the visible region centered at approximately 530 nm (Figure 8). Analogous spectra are obtained from synthetic Fe(II)·(α-keto acid) complexes (*20*−*22*, *25*) where the energy of this spectral feature is easily tuned by varying the substituent on the α-keto acid. Electron-donating groups shift the transition to shorter wavelengths (higher energy), while electron-withdrawing groups shift it to longer wavelengths (lower energy) (*20*, *21*), consistent with its assignment as a metal-to-ligand charge transfer (MLCT) transition from the Fe(II) center to the α-keto acid. Significantly, this feature is only observed when the α-keto acid chelates via the carboxylate oxygen and the α-keto oxygen; when the α-keto acid binds in a monodentate fashion, the model iron complexes remain colorless (*21*, *22*). Thus, this broad absorption feature is diagnostic of an α-keto acid chelated to an Fe(II) metal center, indicating that α-KG chelates to the iron in TfdA.

The MLCT transition observed in the presence of α-KG is a convenient probe for monitoring the binding of the primary substrate 2,4-D. As shown in Figure 8, upon the addition of 2,4-D, the absorption is blue-shifted and the optical spectrum sharpens significantly, revealing the presence of at least three different charge-transfer transitions (λ_{max} = 515 nm with shoulders at approximately 475 and 560 nm). These results indicate that α-KG remains chelated to the Fe(II) center in the presence of substrate [i.e., in the Fe−TfdA·(α-KG)·(2,4-D) complex], and that 2,4-D binding affects the coordination environment of the iron(II) center.

Binding of NO to Fe(II)-Reconstituted TfdA. In an effort to gain insight into O_2 binding at the active site, various

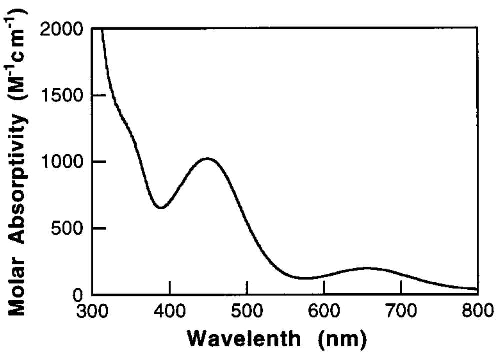

FIGURE 9: Optical absorption spectrum of Fe−TfdA·(α-KG)·(2,4-D)·(NO) (λ_{max} = 449 and 657 nm).

complexes of TfdA were incubated with the O_2 analogue NO. Such an approach has been applied successfully to both model complexes and other iron(II) oxygenases (*58*−*61*). Nitric oxide has an advantage over other O_2-mimics (such as azide) because the radical NO converts the usually nonchromophoric and effectively EPR-silent high-spin (S = 2) Fe(II) ion into an $\{FeNO\}^7$ system (*62*), which is EPR active (S = 3/2) and contains a visible chromophore. Thus, the use of NO provides additional spectroscopic techniques with which to probe the metal center.

Nitric oxide reacts readily with Fe−TfdA, the binary complex Fe−TfdA·(α-KG), and the ternary complex Fe−TfdA·(α-KG)·(2,4-D), as assessed by the formation of characteristic bright yellow iron-nitrosyl species (*58*, *63*). The electronic structure of these complexes appears to be dominated by Fe−NO interactions, since the spectra exhibit only slight variations in the presence/absence of α-KG and 2,4-D [only the Fe−TfdA·(α-KG)·(2,4-D)·(NO) spectrum is shown in Figure 9]. On the basis of detailed spectroscopic analysis of small inorganic Fe−NO model complexes, the absorptions observed at 449 and 657 nm have been assigned by Solomon and co-workers to $NO^- \rightarrow Fe^{3+}$ and Fe^{3+} ligand field transitions, respectively (*63*). The assignment of the TfdA complexes as Fe−NO species was corroborated by EPR spectroscopy (Figure 10), which yielded signals very close to $\mathbf{g}$ = 4, 4, and 2 as expected for axial S = 3/2 systems (*58*). The spectra of Fe−TfdA·(NO) and Fe−TfdA·(α-KG)·(NO) are essentially identical with $\mathbf{g}_x = 4.09$, $\mathbf{g}_y = 3.98$, and $\mathbf{g}_z = 2.00$ and a peak-to-peak width of 6.4 mT in the $\mathbf{g}$ = 4 region. In the presence of both α-KG and 2,4-D, however, the $\{Fe{-}NO\}^7$ center becomes more rhombic, with signals at $\mathbf{g}_x = 4.12$, $\mathbf{g}_y = 3.96$, and $\mathbf{g}_z = 2.00$ and a peak-to-peak width of 8.9 mT. This change is mirrored in the copper EPR data of the ternary Cu−TfdA·(α-KG)·(2,4-D) complex which indicates that the copper ion also is in a more rhombic environment. The binding of NO directly to the ternary Fe−TfdA·(α-KG)·(2,4-D) complex indicates that even in the presence of both α-KG and 2,4-D, an available coordination site is maintained on the iron atom for the binding of NO and, by analogy, O_2. In addition, the fact that NO binds directly to the metal ion implies that O_2 activation occurs via direct ligation of O_2 to the Fe(II) center, not via some outer-sphere electron-transfer pathway. The Fe−TfdA·(α-KG)·(2,4-D)·(NO) complex is the best model to date of the active quaternary Fe−TfdA·(α-KG)·(2,4-D)·(O_2) complex, i.e., the species which ultimately gives rise to catalysis.

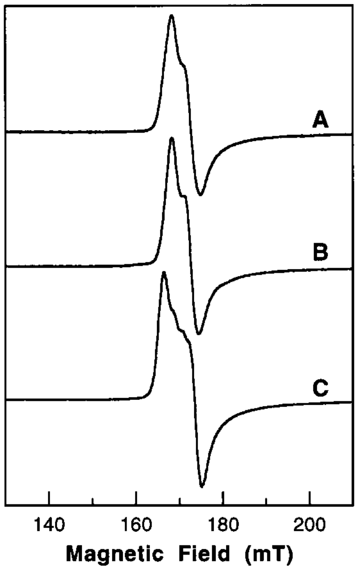

FIGURE 10: EPR spectra of Fe−TfdA-nitrosyl complexes. Only the expanded $\mathbf{g}$ = 4 region is displayed since the $\mathbf{g}$ = 2 region is relatively uninformative and there was frequent overlap with the signal of free NO. (A) Fe−TfdA·(NO) ($\mathbf{g}_x = 4.09$, $\mathbf{g}_y = 3.98$, $\mathbf{g}_z = 2.00$, $\mathbf{g}_x$ to $\mathbf{g}_y$ peak-to-peak width of 6.4 mT); (B) Fe−TfdA·(α-KG)·(NO) ($\mathbf{g}_x = 4.09$, $\mathbf{g}_y = 3.98$, $\mathbf{g}_z = 2.00$, $\mathbf{g}_x$ to $\mathbf{g}_y$ peak-to-peak width of 6.4 mT); (C) Fe−TfdA·(α-KG)·(2,4-D)·(NO) ($\mathbf{g}_x = 4.12$, $\mathbf{g}_y = 3.96$, $\mathbf{g}_z = 2.00$, $\mathbf{g}_x$ to $\mathbf{g}_y$ peak-to-peak width of 8.9 mT).

NO binding appears to be reversible under certain circumstances as evidenced by the frequent presence of free NO in the EPR spectra of both Fe−TfdA·(NO) and Fe−TfdA·(α-KG)·(NO). To further characterize the reversibility of NO binding, optical spectra of various nitrosyl complexes were monitored as the complexes were placed under gentle vacuum followed by incubation under an argon atmosphere. The results demonstrated that NO does, in fact, bind reversibly to both the Fe−TfdA and Fe−TfdA·(α-KG) complexes (most NO exchanged within 10 min). Under these same conditions, however, NO was *not* released from the ternary Fe−TfdA·(α-KG)·(2,4-D) complex. This increased affinity for NO, and by analogy O_2, in the presence of substrate(s) was observed previously in other O_2-activating non-heme Fe(II) enzymes (*59*, *60*) and presumably protects the enzyme from self-inactivation since the formation of reactive Fe−O_2 species is controlled.

DISCUSSION

TfdA exhibits many features associated with the emerging class of mononuclear non-heme iron enzymes that possess a 2-His-1-carboxylate facial triad (*19*). While these enzymes activate dioxygen to catalyze a diverse array of oxidative transformations, they share a common structural motif in which two histidines and one carboxylate occupy a trigonal face of the metal coordination sphere (Figure 1). This facial triad is proposed to anchor the iron(II) center in the active site, leaving the remaining coordination sites available for binding exogenous ligands such as cofactor, substrate, and/or O_2 (*19*). Such an arrangement allows the enzyme to juxtapose reactants to facilitate catalysis. In addition, it has been suggested that ligating anionic exogenous ligands may prime the iron center for binding and activating O_2, presumably by altering the redox potential of the metal center (*19*). Scheme 4 shows a proposed mechanistic scheme for TfdA based on our results as well as information from other mechanistically related enzymes and model systems (*2*, *8*, Scheme 4: Proposed Reaction Scheme for TfdA Based on Current TfdA Studies and Published Work with Related Enzymes

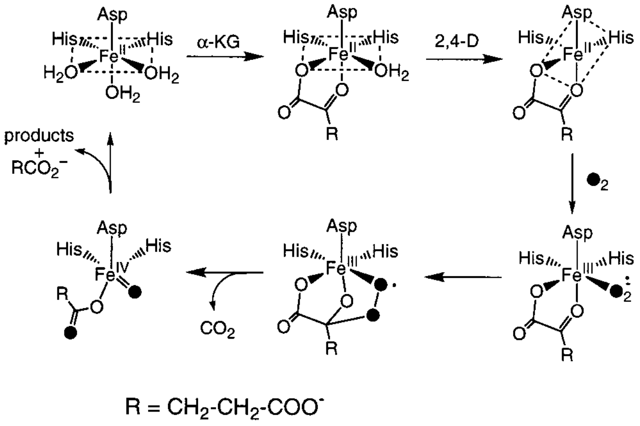

9, *20*−*25*, *31*). Evidence supporting this scheme is discussed in the following sections.

2-His-1-Carboxylate Facial Triad. Our EPR and ESEEM studies of Cu−TfdA and the binary Cu−TfdA·(α-KG) complex demonstrate that two histidine ligands coordinate the metal center in the equatorial plane. In the EPR spectra, both the lowest $\mathbf{g}_{\parallel}$ feature and the $\mathbf{g}_{\perp}$ signal exhibit 5-fold splitting, indicative of superhyperfine splitting from two nitrogen ligands. These two nitrogen ligands were identified on the basis of characteristic ESEEM features as arising from the distal nitrogens of two or more coordinated histidine ligands (*32*). The present results are consistent with extended X-ray absorption fine structure (EXAFS) spectroscopic data (*31*) that identified two histidine ligands to both the Cu−TfdA and the Fe−TfdA metallocenters.

Sequence comparisons show that IPNS and a subset of the α-keto acid-dependent enzymes share a common His-X-Asp-X$_{(53-57)}$-His motif (*30*). On the basis of numerous spectroscopic and biochemical studies, it was proposed that this motif provides the endogenous ligands to the metal center (*19*), a notion later confirmed crystallographically for IPNS (*18*) and DAOCS (*8*, *9*). TfdA also contains a His-X-Asp-X$_{51}$-His sequence (His113, Asp115, and His167) (*29*), although it does *not* possess obvious overall sequence similarity to IPNS or DAOCS. Furthermore, mutagenesis studies on TfdA have demonstrated that the residues associated with this motif are essential for enzyme activity.[3] Together with the EPR, ESEEM, and EXAFS data, these results provide very strong evidence that TfdA utilizes the 2-His-1-carboxylate facial triad as the endogenous metal ligand set.

Exogenous Ligands. A key aspect of the 2-His-1-carboxylate facial triad is that this endogenous ligand set maintains three cis-oriented sites which are available for the binding of exogenous ligands and are proposed to play a critical role in the catalytic mechanisms of these enzymes (*19*). By analogy to DAOCS (*9*), these sites are presumably occupied by solvent molecules in the resting state of TfdA. Indeed, ESEEM spectroscopic results of Cu−TfdA in H_2O and D_2O are consistent with the presence of one axial and two equatorial water molecules. Significantly, the EPR spectrum of Cu−TfdA obtained in the presence of imidazole buffer shows evidence for imidazole binding to the metal center, presumably displacing one or two solvent molecules from the principal tetragonal plane.

The addition of the cosubstrate α-KG to Fe(II)-reconstituted TfdA results in the displacement of two coordinating solvent ligands as shown by the development of MLCT transitions that are diagnostic of an α-keto acid moiety chelated to an Fe(II) center (*20*−*22*, *25*). Indeed, the crystal structure of the Fe-DAOCS·(α-KG) complex reveals just such a chelated α-KG (*9*). A chelated α-KG was also recently deduced for the Fe(II)-reconstituted α-keto acid-dependent enzymes CS2 (*23*) and TauD (*64*).[4] Thus, the chelate binding mode of α-KG appears to be general to all α-keto acid-dependent enzymes. The proposed binding orientation for α-KG shown in Scheme 4 corresponds to that observed in the crystal structure of DAOCS.

The optical spectrum of the ternary Fe−TfdA·(α-KG)·(2,4-D) complex retains MLCT transitions characteristic of an α-keto acid chelated to an Fe(II) ion, indicating that α-KG remains chelated to the iron center in the presence of the substrate 2,4-D. The addition of substrate does, however, alter the coordination environment of the active site as evidenced by the blue-shift in the MLCT transitions and the sharpening of the optical spectrum. Analogous perturbations to the MLCT transitions also occur in the spectra of both Fe−CS2·(α-KG) (*24*) and Fe−TauD·(α-KG) (*64*) upon addition of the appropriate substrate, suggesting that this perturbation may be a feature common to all α-keto acid-dependent enzymes. We interpret the sharpening of the optical features as an indication that the iron is in a more homogeneous environment in the presence of both α-KG and 2,4-D, and that the Fe(II) ion is now “locked” in position and primed for catalysis.

In contrast to the Fe(II)-reconstituted enzyme, addition of α-KG to Cu(II)-substituted TfdA results in the displacement of only a single equatorial water molecule according to ESEEM analysis, suggesting that α-KG binds in a monodentate fashion to Cu−TfdA. This difference in α-keto acid-binding mode between Cu(II) and Fe(II) adducts, which has also been observed in model complexes (*65*), is not surprising given the preference of Cu(II) to maintain a tetragonal coordination environment. Upon the addition of 2,4-D to the Cu−TfdA·(α-KG) complex, a second equatorial water molecule is lost. It remains unclear whether the water is displaced by the α-keto group or by direct ligation of the substrate, but we favor the former interpretation which would allow the primary substrate to bind identically in the Cu- and Fe-enzymes.

Creation of an O_2-Binding Site. As illustrated in Scheme 4, one feature associated with priming the Fe(II) site for reaction with O_2 may entail the loss of a ligand to form a coordinately unsaturated metal center. Our EPR studies of various Cu−TfdA and nitrosyl-Fe−TfdA complexes indicate that a significant change occurs in the metal environment upon formation of the Cu/(Fe−NO)−TfdA·(α-KG)·(2,4-D) complex, with both spectra exhibiting more rhombicity. In addition, for Cu−TfdA·(α-KG)·(2,4-D), we observe a low field shift of $\mathbf{g}_{\parallel}$ to 2.37, a decrease of $A_{\parallel}$ to 12.0 mK, and a

---

[3] Hogan, D. A., Smith, S. R., Saari, E. A., McCracken, J., and Hausinger, R. P., manuscript in preparation.

[4] TauD catalyzes the conversion of taurine to aminoacetaldehyde and sulfite [Eichhorn et al. (1997) *J. Biol. Chem. 272*, 23031−23036].

sharpening of the $\mathbf{g}_{\|}$ signals by a factor of 2 due to the loss of superhyperfine splitting from one nitrogen ligand. The first two spectral changes indicate a Cu(II) ion with more oxyanionic ligands in the principal tetragonal plane (*44*), while the third indicates the displacement of one His ligand from this plane (shown by the shift in position of the dotted lines in Scheme 4). Two options can be considered for this His displacement: complete loss of a His ligand from the coordination sphere or a reorientation of the principal **g**-tensor axis.

In support of a model in which one His ligand is lost upon addition of the substrate 2,4-D, EXAFS spectra of the ternary Cu−TfdA•(α-KG)•(2,4-D) and binary Fe−TfdA•(2,4-D) complexes show decreases in the intensity of outer-sphere features due to imidazole coordination (*31*). It should be stressed, however, that precise numbers of ligands are difficult to assign by this method, especially involving second-shell atoms, and that EXAFS spectra for the ternary Fe−TfdA•(α-KG)•(2,4-D) complex were not reported (*31*). The EXAFS data suggest that 2,4-D binding leads to His displacement but do not define whether the ligand changes arise from protein conformational changes associated with substrate binding or whether the carboxylate of 2,4-D replaces the endogenous ligands. In the latter case, this proposed displacement would be specific only for substrates with carboxylate groups and not apply to either prolyl hydroxylase or lysyl hydroxylase, two α-keto acid-dependent enzymes involved in collagen formation (*1*). A further argument against this model is the crystal structure reported for DAOCS. If the active site of DAOCS is representative of that in TfdA, the displacement of a histidine in the facial triad would appear to require substantial side-chain rearrangements (*8*, *9*).

We currently favor an alternative interpretation in which the endogenous 2-His-1-carboxylate facial triad is maintained upon 2,4-D binding. According to this alternative proposal, α-KG binds iron in a chelate fashion while 2,4-D binds in a pocket near the iron center and induces the loss of a solvent molecule from the metal coordination sphere, resulting in a 5-coordinate iron(II) metallocenter. This interpretation is in agreement with the perturbation observed at the iron(II) center upon addition of 2,4-D to Fe−TfdA•(α-KG), as well as the crystal structure (*9*) and modeled substrate binding pocket (*8*) of DAOCS. Further support of this model is provided by detailed spectroscopic studies of CS2 (*23*, *24*) in which Solomon and co-workers demonstrated a shift from a 6- to 5-coordinate Fe(II) center upon substrate binding. In the case of Cu−TfdA, we propose that the interactions with α-KG and 2,4-D cause a reorientation of the principal tetragonal plane in Cu−TfdA, resulting in a shift of one of the histidines from the tetragonal plane to an axial position (Scheme 4). This reorientation increases the number of oxygen ligands in this plane and decreases the multiplicity of the superhyperfine splitting, consistent with the Cu−TfdA EPR data.

As Scheme 4 illustrates, having formed the ternary Fe−TfdA•(α-KG)•(2,4-D) complex, the next step is to bind O_2. Evidence that the addition of substrate to the binary complex primes the iron to bind and activate O_2 can be derived from studies with the O_2 mimic NO. Nitric oxide binding is reversible unless both α-KG and 2,4-D are present, suggesting that the ternary complex has a much higher affinity than the binary or free enzyme for NO and, by analogy, O_2. An energetic coupling of NO/O_2 and substrate binding has been observed previously in other non-heme iron enzymes that activate O_2, including three different extradiol dioxygenases (*59*, *60*) and IPNS (*61*). The increased affinity for NO/O_2 only in the presence of a properly "primed" active site presumably serves to protect the enzyme since the potent oxidizing species will only be generated when the catalytic cycle can be completed (*19*). This hypothesis is consistent with the ordered binding mechanism established for the α-keto acid-dependent enzyme thymine 7-hydroxylase (*4*), where O_2 binds after both α-KG and the primary substrate and the fact that the oxidative decarboxylation of α-KG cannot be uncoupled from 2,4-D oxidation in TfdA (*27*). In addition, stopped-flow studies with TauD demonstrate an enhanced rate of reaction with O_2 for the ternary complex relative to Fe−TauD•(α-KG), suggesting a similar priming of the active site upon the addition of both α-KG and the primary substrate (*64*).

Mechanistic Considerations. Understanding the coordination environment of the iron(II) center in TfdA ultimately leads to the question of how α-keto acid-dependent enzymes activate O_2. Cytochrome P-450, the prototypical heme oxygenase, utilizes an electron from NADH and one from the porphyrin ring itself to generate compound I, the putative high valent iron−oxo species involved in oxidation (*66*). In the non-heme methane monooxygenase, the dinuclear iron activates O_2 to form intermediate Q, proposed to be a diiron(IV)-oxo species (*67*). Mononuclear, non-heme iron enzymes, however, must utilize the exogenous ligands themselves to supply the additional electrons necessary to activate and reduce O_2 (*19*). Thus, the extra electrons are furnished by the cosubstrate α-KG in α-keto acid-dependent enzymes. Still left unanswered, however, is how these enzymes overcome the energy required to break the O−O bond. In heme enzymes, it is generally accepted that O−O bond cleavage is induced by the "push−pull" mechanism, with the respective involvement of the proximal and distal residues (*66*). No such mechanism is available in the α-keto acid-dependent oxygenases. Analysis of the reactivity of model complexes suggests that the oxidative decarboxylation itself may provide the necessary driving force; that is, the loss of CO_2 may be coupled to O−O bond cleavage as depicted in Scheme 4 and, therefore, provides the energy required to overcome this key activation barrier (*20*). Thus, the α-keto acid cosubstrate would have a unique role, providing both electrons and an energetic boost.

In conclusion, the spectroscopic results reported herein have greatly expanded our knowledge of the iron coordination environment in α-keto acid-dependent enzymes. Our current working model for TfdA, shown in Scheme 4, builds on a hypothetical mechanism first proposed for prolyl hydroxylase by Hanauske-Abel in 1982 (*26*). The scheme consists of an iron coordinated to the active site via the widely used 2-His-1-carboxylate facial triad with the remaining sites filled with solvent molecules and available for the binding of exogenous ligands. α-KG chelates to the iron via the α-keto oxygen and a carboxylate oxygen forming a stable five-membered ring. This binding mode is maintained even in the presence of the primary substrate 2,4-D, the binding of which induces the loss of a solvent ligand to generate a 5-coordinate iron(II) center. Upon the binding of O_2 at the vacant site, α-KG is oxidatively decarboxylated, releasing both the electrons and the driving force necessary to form the putative high valent iron−oxo intermediate. Thus, the unique coordination environment of α-keto acid-dependent enzymes affords an oxygen activation mechanism, which is distinct from those utilized by oxygenases which require a porphyrin ring or a second metal ion.

REFERENCES

1. Abbott, M. T., and Udenfriend, S. (1974) in Molecular Mechanisms of Oxygen Activation (Hayaishi, O., Ed.) pp 167−214, Academic Press, New York.
2. Que, L., Jr., and Ho, R. Y. N. (1996) *Chem. Rev. 96*, 2607−2624.
3. Prescott, A. G., and John, P. (1996) *Annu. Rev. Plant Physiol. Plant Mol. Biol. 47*, 245−271.
4. Holme, E. (1975) *Biochemistry 14*, 4999−5003.
5. De Carolis, E., and De Luca, V. (1993) *J. Biol. Chem. 268*, 5504−5511.
6. Myllylä, R., Tuderman, L., and Kivirikko, K. I. (1977) *Eur. J. Biochem. 80*, 349−357.
7. Puistola, U., Turpeenniemi-Hujanen, T. M., Myllylä, R., and Kivirikko, K. I. (1980) *Biochim. Biophys. Acta 611*, 51−60.
8. Lloyd, M. D., Lee, H.-J., Harlos, K., Zhang, Z.-H., Baldwin, J. E., Schofield, C. J., Charnock, J. M., Garner, C. D., Hara, T., van Scheltinga, A. C. T., Valegård, K., Viklund, J. A. C., Hajdu, J., Andersson, I., Danielsson, Å., and Bhikhabhai, R. (1999) *J. Mol. Biol. 287*, 943−960.
9. Valegård, K., van Scheltinga, A. C. T., Lloyd, M. D., Hara, T., Ramaswamy, S., Perrakis, A., Thompson, A., Lee, H.-J., Baldwin, J. E., Schofield, C. J., Hajdu, J., and Andersson, I. (1998) *Nature 394*, 805−809.
10. Serre, L., Sailland, A., Sy, D., Boudec, P., Rolland, A., Pebay-Peyroula, E., and Cohen-Addad, C. (1999) *Structure 7*, 977−988.
11. Senda, T., Sugiyama, K., Narita, H., Yamamoto, T., Kimbara, K., Fukuda, M., Sato, M., Yano, K., and Mitsui, Y. (1996) *J. Mol. Biol. 255*, 735−752.
12. Han, S., Eltis, L. D., Timmis, K. N., Muchmore, S. W., and Bolin, J. T. (1995) *Science 270*, 976−980.
13. Kita, A., Kita, S., Fujisawa, I., Inaka, K., Ishida, T., Horiike, K., Nozaki, M., and Miki, K. (1999) *Structure 7*, 25−34.
14. Sugimoto, K., Senda, T., Aoshima, H., Masai, E., Fukuda, M., and Mitsui, Y. (1999) *Structure 7*, 953−965.
15. Goodwill, K. E., Sabatier, C., and Stevens, R. C. (1998) *Biochemistry 37*, 13437−13445.
16. Erlandsen, H., Flatmark, T., Stevens, R. C., and Hough, E. (1998) *Biochemistry 37*, 15638−15646.
17. Kauppi, B., Lee, K., Carredano, E., Parales, R. E., Gibson, D. T., Eklund, H., and Ramaswamy, S. (1998) *Structure 6*, 571−586.
18. Roach, P. L., Clifton, I. J., Hensgens, C. M. H., Shibata, N., Schofield, C. J., Hajdu, J., and Baldwin, J. E. (1997) *Nature 387*, 827−830.
19. Hegg, E. L., and Que, L., Jr. (1997) *Eur. J. Biochem. 250*, 625−629.
20. Hegg, E. L., Ho, R. Y. N., and Que, L., Jr. (1999) *J. Am. Chem. Soc. 121*, 1972−1973.
21. Chiou, Y.-M., and Que, L., Jr. (1995) *J. Am. Chem. Soc. 117*, 3999−4013.
22. Hikichi, S., Ogihara, T., Fujisawa, K., Kitajima, N., Akita, M., and Moro-oka, Y. (1997) *Inorg. Chem. 36*, 4539−4547.
23. Pavel, E. G., Zhou, J., Busby, R. W., Gunsior, M., Townsend, C. A., and Solomon, E. I. (1998) *J. Am. Chem. Soc. 120*, 743−753.
24. Zhou, J., Gunsior, M., Bachmann, B. O., Townsend, C. A., and Solomon, E. I. (1998) *J. Am. Chem. Soc. 120*, 13539−13540.
25. Ha, E. H., Ho, R. Y. N., Kosiel, J. F., and Valentine, J. S. (1995) *Inorg. Chem. 34*, 2265−2266.
26. Hanauske-Abel, H. M., and Günzler, V. (1982) *J. Theor. Biol. 94*, 421−455.
27. Fukumori, F., and Hausinger, R. P. (1993) *J. Biol. Chem. 268*, 24311−24317.
28. Fukumori, F., and Hausinger, R. P. (1993) *J. Bacteriol. 175*, 2083−2086.
29. Streber, W. R., Timmis, K. N., and Zenk, M. H. (1987) *J. Bacteriol. 169*, 2950−2955.
30. Borovok, I., Landman, O., Kreisberg-Zakarin, R., Aharonowitz, Y., and Cohen, G. (1996) *Biochemistry 35*, 1981−1987.
31. Cosper, N. J., Stålhandske, C. M. V., Saari, R. E., Hausinger, R. P., and Scott, R. A. (1999) *J. Biol. Inorg. Chem. 4*, 122−129.
32. Whiting, A. K., Que, L., Jr., Saari, R. E., Hausinger, R. P., Fredrick, M. A., and McCracken, J. (1997) *J. Am. Chem. Soc. 119*, 3413−3414.
33. Fasman, G. D., Ed. (1976) *Handbook of Biochemistry and Molecular Biology*, CRC Press, Inc, CRC Press, Inc, Boca Raton, FL.
34. Saari, R. E., and Hausinger, R. P. (1998) *Biochemistry 37*, 3035−3042.
35. Belford, R. L., and Belford, G. G. (1973) *J. Chem. Phys. 59*, 853−854.
36. Cammack, R., and Cooper, C. E. (1993) *Methods Enzymol. 227*, 353−384.
37. McCracken, J., Shin, D.-H., and Dye, J. L. (1992) *Appl. Magn. Reson. 3*, 305−316.
38. Lin, C. P., Bowman, M. K., and Norris, J. R. (1985) *J. Magn. Reson. 65*, 369−374.
39. Britt, R. D., and Klein, M. P. (1987) *J. Magn. Reson. 74*, 535−540.
40. Mims, W. B. (1984) *J. Magn. Reson. 59*, 291−306.
41. Mims, W. B. (1972) *Phys. Rev. B 5*, 2409−2419.
42. Bertini, I., and Scozzafava, A. (1981) *Metal Ions Biol. Sys. 12*, 31−74.
43. Solomon, E. I., Baldwin, M. J., and Lowery, M. D. (1992) *Chem. Rev. 92*, 521−542.
44. Peisach, J., and Blumberg, W. E. (1974) *Arch. Biochem. Biophys. 165*, 691−708.
45. Rosenberg, R. C., Root, C. A., Bernstein, P. K., and Gray, H. B. (1975) *J. Am. Chem. Soc. 97*, 2092−2096.
46. Addison, A. W. (1983) in *Copper Coordination Chemistry: Biochemical and Inorganic Perspectives* (Karlin, K. D., and Zubieta, J., Eds.) pp 109−128, Adenine Press, New York.
47. Styring, S., and Brändén, R. (1985) *Biochemistry 24*, 6011−6019.
48. Dickinson, L. C., Rose, S. L., and Westhead, E. W. (1980) *J. Inorg. Biochem. 13*, 353−366.
49. Andersson, I. (1996) *J. Mol. Biol. 259*, 160−174.
50. Larsen, T. M., Wedekind, J. E., Rayment, I., and Reed, G. H. (1996) *Biochemistry 35*, 4349−4358.
51. Coulter, E. D., Moon, N., Batie, C. J., Dunham, W. R., and Ballou, D. P. (1999) *Biochemistry 38*, 11062−11072.
52. Rowan, L. G., Hahn, E. L., and Mims, W. B. (1965) *Phys. Rev. 137*, A61−A71.
53. Dikanov, S. A., Shubin, A. A., and Parmon, V. N. (1981) *J. Magn. Reson. 42*, 474−487.
54. Mims, W. B., Davis, J. L., and Peisach, J. (1984) *Biophys. J. 45*, 755−766.
55. McCracken, J., Peisach, J., and Dooley, D. M. (1987) *J. Am. Chem. Soc. 109*, 4064−4072.
56. Atherton, N. M., and Horsewill, A. J. (1979) *Mol. Phys. 37*, 1349−1361.
57. Kevan, L., Bowman, M. K., Narayana, P. A., Boeckman, R. K., Yudanov, V. F., and Tsvetkov, L. (1975) *J. Chem. Phys. 63*, 409−416.
58. Chiou, Y.-M., and Que, L., Jr. (1995) *Inorg. Chem. 34*, 3270−3278.
59. Wolgel, S. A., Dege, J. E., Perkins-Olson, P. E., Juarez-Garcia, C. H., Crawford, R. L., Münck, E., and Lipscomb, J. D. (1993) *J. Bacteriol. 175*, 4414−4426.

60. Arciero, D. M., Orville, A. M., and Lipscomb, J. D. (1985) *J. Biol. Chem. 260*, 14035−14044.
61. Chen, V. J., Orville, A. M., Harpel, M. R., Frolik, C. A., Surerus, K. K., Münck, E., and Lipscomb, J. D. (1989) *J. Biol. Chem. 264*, 21677−21681.
62. Feltham, R. D., and Enemark, J. H. (1981) *Top. Stereochem. 12*, 155−215.
63. Brown, C. A., Pavlosky, M. A., Westre, T. E., Zhang, Y., Hedman, B., Hodgson, K. O., and Solomon, E. I. (1995) *J. Am. Chem. Soc. 117*, 715−732.
64. Ryle, M. J., Padmakumar, R., and Hausinger, R. P. (1999) *Biochemistry 46*, 15278−15286.
65. Zheng, H., and Que, L., Jr. (1997) *Inorg. Chim. Acta 263*, 301−307.
66. Sono, M., Roach, M. P., Coulter, E. D., and Dawson, J. H. (1996) *Chem. Rev. 96*, 2841−2887.
67. Wallar, B. J., and Lipscomb, J. D. (1996) *Chem. Rev. 96*, 2625−2657.

BI991796L